Applied Catalysis B: Environmental 248 (2019) 423–429

Contents lists available at ScienceDirect

Applied Catalysis B: Environmental

journal homepage: www.elsevier.com/locate/apcatb

Combination of polyoxotantalate and metal sulfide: A new-type noble-metal-free binary photocatalyst $Na_8Ta_6O_{19}/Cd_{0.7}Zn_{0.3}S$ for highly efficient visible-light-driven H_2 evolution

XueJun Zhou[a,b], Hao Yu[a], Dan Zhao[c], XinChen Wang[a,*], ShouTian Zheng[a,*]

[a] State Key Laboratory of Photocatalysis on Energy and Environment, College of Chemistry, Fuzhou University, Fuzhou, Fujian, 350108, China
[b] Analysis and Testing Central Facility, Anhui University of Technology, Maanshan, Anhui, 243002, China
[c] Fuqing Branch of Fujian Normal University, Fuqing, Fujian, 350300, China

ARTICLE INFO

Keywords:
Polyoxotantalate
Composite photocatalyst
Visible-light
Hydrogen evolution

ABSTRACT

Polyoxometalates have been emerged in the field of photocatalytic hydrogen evolution reaction (HER) with attempt to get efficient, inexpensive, recyclable, and environmentally-benign photocatalysts. Here, it demonstrated that the combination of polyoxotantalates with metal sulfides can form none-noble-metal binary composite photocatalysts for efficient water splitting with visible-light. With the strategy, the first series of noble-metal-free composite photocatalysts based on the combination of hexatantalate $Na_8Ta_6O_{19}$ and metal sulfide $Cd_xZn_{(1-x)}S$ have been prepared and used as a heterogeneous photocatalyst. The $Na_8Ta_6O_{19}/Cd_xZn_{(1-x)}S$ exhibits efficient hydrogen production activity, even without any cocatalysts. The maximum H_2-evolution rate reaches 43.05 mmol h^{-1} g^{-1} (based on 10 mg catalyst) with the apparent quantum yield of 37% at 420 nm, which is the highest value ever reported so far for polyoxometalate-based photocatalysts to our knowledge. The achievement provides a new strategy to develop highly efficient and new-type photocatalysts for the sustainable utilization of solar energy by merging polyoxotantalate chemistry with photoredox catalysis.

1. Introduction

The search for highly efficient and stable photocatalysts for photocatalytic water splitting under visible light irradiation has been ragarded as a huge challenging and very important research topic due to the tremendous energy crisis and growing environmental pollution problems over the past few decades [1–4]. Various inorganic and organic semiconductor photocatalysts including metal oxides, metal sulfides and graphitic carbon nitride [5–12] have been investigated in this field, but their relatively low charge separation efficiency, insufficient surface catalytic reactions and only absorption of ultraviolet (UV) light significantly retard their practical applications.The synthesis of visible light responsive photocatalyst with excellent charge separation ability and high solution stability still remains as a challenge.

Among numberous semiconductor photocatalysts developed in the past several decades, sulphide catalysts have been intensively studied due to their favourable band gaps and excellent catalytic functions. Especially, CdS has been considered to be an efficient photocatalyst due to its high-effcient photoconversion ability and suitable conduction band energy level. Nevertheless, the intrinsic drawbacks, such as the photocorrosion and insufficient charge separation [5], have limited their further development. Modifying CdS by incorporating other metals with d^{10} electronic configuration to form solid state solution has been applied to handle the above issue. For example, mixed-metal sulfides $Cd_xZn_{(1-x)}S$ have been proven to be a cost-effective and efficient visible-light-responsive photocatalysts [13–16].Nevertheless, the H_2-production activity of the $Cd_xZn_{(1-x)}S$ photocatalysts is far from satisfactory. In order to promote the activity and improve the stability of a metal sulfide catalyst, various co-catalysts have been loaded on metal sulfides [17–22]. The co-catalysts can extract the photogenerated charge carriers from the catalysts and thus inhibiting the recombination of photogenerated electron–hole pairs.

Polyoxometalates (POMs) with high oxidation-states have captured sustainable interests owing to their charming structural vairations together with promising utilizations on photochemistry and electrochemistry [23–26]. They can act as an excellent electron reservoir, which can undergo multiple electron transfer reaction processes and maintain the structure well. Thus, POMs are ideal electron scavengers to capture the photogenerated electrons in the conduction band (CB) of a semiconductor to improve the separation efficiency of photogenerated

* Corresponding authors.
E-mail addresses: xcwang@fzu.edu.cn (X. Wang), stzheng@fzu.edu.cn (S. Zheng).

https://doi.org/10.1016/j.apcatb.2019.02.052
Received 11 December 2018; Received in revised form 30 January 2019; Accepted 18 February 2019
Available online 19 February 2019
0926-3373/

carriers. To date, various POM-based catalysts have been prepared for photocatalytic H_2 evolution [27–33]. However, the majority of reported POM-based photocatalysts is either operated under ultraviolet irradiation or contains noble metal as a cocatalyst or a photosensitizer. In addition, the H_2-production rates of most of POM-based photocatalysts are below 10 mmol h^{-1} g^{-1}.Therefore, the development of new-type, visible-light-responsive, and highly-active POM-based photocatalysts is desired.

The integration of POMs with $Cd_xZn_{(1-x)}S$ photocatalyst may overcome the disadvantages of $Cd_xZn_{(1-x)}S$ with fast electron–hole recombination rate and low surface area. Polyoxotantalates (POTas), as a burgeoning subclass of POMs, have attracted increasing interest because of their high specific surface area, high charge, high alkalinity, and photocatalytic activity. Thus, it is very interesting to combine polyoxotantalates with $Cd_xZn_{(1-x)}S$ to produce high-performance composite photocatalytic materials.

Here, we represents the our attempt on combining POTa with metal sulfide via a hydrothermal method to get new-type binary $Na_8Ta_6O_{19}$/$Cd_{0.7}Zn_{0.3}S$ (Ta_6/CZS) composite photocatalysts for potocatalytic H_2 evolution. Fascinatingly, the results reveal that the composite photocatalysts Ta_6/CZS show a series of rare POM-based noble-metal free photocatalysts that can catalyze H_2 evolution from water under visible light irradiation. Especially, by the synergetic effect between CZS and Ta_6 of Ta_6/CZS photocatalysts, the photo-generated electrons and holes can be efficiently separated to exhibit outstanding photocatalytic H_2-production activity. Notably, without any cocatalyst, the maximum H_2 evolution rate of Ta_6/CZS photocatalysts is up to 43.05 mmol h^{-1} g^{-1}, which is higher than those of all known POM- based photocatalyts and most known metal-sulfide-based photocatalyts for visible-light-driven H_2 evolution.

2. Experimental

2.1. Sample preparation

$Na_8Ta_6O_{19}$ was prepared according to the reported methods in the literature with a little modification [34]. Other reagents were of analytical grade and were used without further purification. In a typical synthesis of the Ta_6-n/CZS composite photocatalysts, 4.2 mmol of Cd$(CH_3COO)_2{\cdot}2H_2O$ and 1.8 mmol of Zn$(CH_3COO)_2{\cdot}2H_2O$ were dissolved into 15 mL of mixed solvent composed of distilled water (10 mL) and 5 mL of Diethylenetriamine(DETA). After being stirred for 5 min, 12 mmol of L-cystine was mixed into the above liquor. The mixture liquor was further stirred for 30 min, then a certain amount of $Na_8Ta_6O_{19}$ (0.025, 0.05, 0.1, 0.25, 0.5, 0.75,1.0 g) was dispersed into the above mixed solution to form a suspension, which was vigorously stirred for 1 h and then was transferred into a 25 mL Teflon-lined stainless autoclave, which was heated to 160 °C for 24 h. The product was cooled to room temperature naturally and then centrifuged and washed with distilled water and ethanol three times and dried at 60 °C overnight in a vacuum oven. For ease of description, as-prepared products with different amounts of $Na_8Ta_6O_{19}$ were named as Ta_6-1/CZS to Ta_6-7/CZS. In addition, pure CZS was also prepared by a similar method without adding $Na_8Ta_6O_{19}$. 2.2.

2.2. Characterization

Fourier transform infrared (FTIR) spectroscopy was recorded in the range 4000-400 cm^{-1} on Nicolet IS50 Fourier transform infrared (FT/IR) spectrometer. Powder X-ray diffraction (PXRD) measurements were recorded on a Ultima IV diffractometer with Cu-*Kα* radiation (λ = 1.5418 Å) in the range 10 – 60°. UV–vis diffused reflectance spectra of the samples were obtained using a UV–vis spectrophotometer (UV-2600) equipped with an integrating sphere attachment and $BaSO_4$ as reference. Morphology and structure were studied with a Transmission electron microscopy (JEOL TEM 2100) as well as a high-resolution transmission electron microscope (HRTEM). The chemical compositions and elemental mappings of the samples were determined by Oxford INCA Energy 350 energy-dispersive X-ray spectrometer equipped on TEM. The metal compositions in the photocatalysts were measured using ICP-AES (ICPS9820). BET surface area was measured by N_2 adsorption and desorption at 77 K using a Micromeritics ASAP2020. All samples were degassed at 150 °C for 12 h in vacuum before analysis. X-ray photoelectron spectroscopy (XPS) was carried out on an ESCALAB 250 spectrometer with an Al-Ka (1486.6 eV) achromatic X-ray source. The photoluminescence spectra were determined at room temperature by an Edinburgh FLS 960 fluorescence spectrometer.

2.3. Photocatalytic hydrogen generation

The hydrogen evolution performance was analysed by a Pyrex reactor connected to the closed gas circulation and evacuation system. 10 mg of as-prepared samples were suspended in 100 mL of aqueous solution including Na_2S (0.35 M) and Na_2SO_3 (0.35 M) as the sacrificial agent. The reactor was degassed and irradiated under 300 W Xe lamp (PLS-SXE 300, Beijing Perfectlight Co. Ltd.) coupled with an UV cut-off filter (λ ≥ 420 nm). The temperature of the working solution was maintained at 278 K under a flow of circulating water. The amount of evolved hydrogen was measured by a gas chromatograph (GC 7900) with a thermal conductivity detector (TCD). The photocatalytic performance of different catalysts was evaluated by the average rate of H_2 evolution in the initial 6 h. After reaction, the catalyst was separated by centrifugation, washed with water several times, and dried at 60 °C in an avacuum oven prior to use for characterization.

The apparent quantum Yield (AQY) was measured under the same photocatalytic reaction condition(10 mg of catalysts mixed with 100 ml of 0.35 M Na_2S/Na_2SO_3), with a monochromatic irradiation light at 420 nm by using band-pass filter and 300 W Xenon lamp. The AQY was calculated according to Equation:

$$AQY\% = \frac{\text{number of reacted electrons}}{\text{number of incident photons}} \times 100\%$$

$$= \frac{2 \text{ number of } H_2 \text{ moleclues evolved}}{\text{number of incident photons}} \times 100\%$$

$$= \frac{2n_{H2}}{n_p} \times 100\%$$

$$n_p = \frac{\theta}{hv} = \frac{I \times t \times A}{hv}$$

where n_p is the number of incident photos, nH_2 is the number of evolved H_2 molecules, θ is the total energy (J) of incident photons, h is the Planck constant (J s^{-1}), ν is the frequency of photo (Hz), I is the illumination intensity (W m^{-2}) determined with a Ray virtual radiation actinometer, t is irradiation time (s), A is the irradiation area (cm^2). The amount of H_2 molecules generated within 1 h is 0.167 mmol. The average intensity of irradiation is determined to be 38.0 mW cm^{-2} by a FZ-A optical power meter and the irradiation area is 4 .8 cm^2.

2.4. Photoelectrochemical measurements

PEC measurements were carried out using a CHI 660E electrochemical workstation (Shanghai Chenhua Instrument Corp., China) in a conventional three electrode system (Ag/AgCl electrode reference electrode and Pt foil counter electrode). The working photoanodes were fabricated as follows: 10 mg Ta_6 /CZS sample was dispersed into 0.5 ml EtOH, and 20 μl nafion(with a concentration of 5 vol%) were mixed by sonication for 30 min to make a slurry. The slurry was then dip-coated onto an FTO glass substrate. (1 cm × 4 cm) and naturally dried under ambient conditions. 0.2 M Na_2SO_4 solution was used as the electrolyte. A 300 W Xe lamp (PLS-SXE300, Perfect Light Company, Beijing, China) coupled with an UV cut-off filter (λ ≥ 420 nm) was utilized as the light source. The photoresponsive signals of the samples were measured under chopped light at 0.0 V. Electrochemical impedance spectra (EIS) were carried out in 0.1 M $K_3[Fe(CN)_6]$ solution in the frequency range

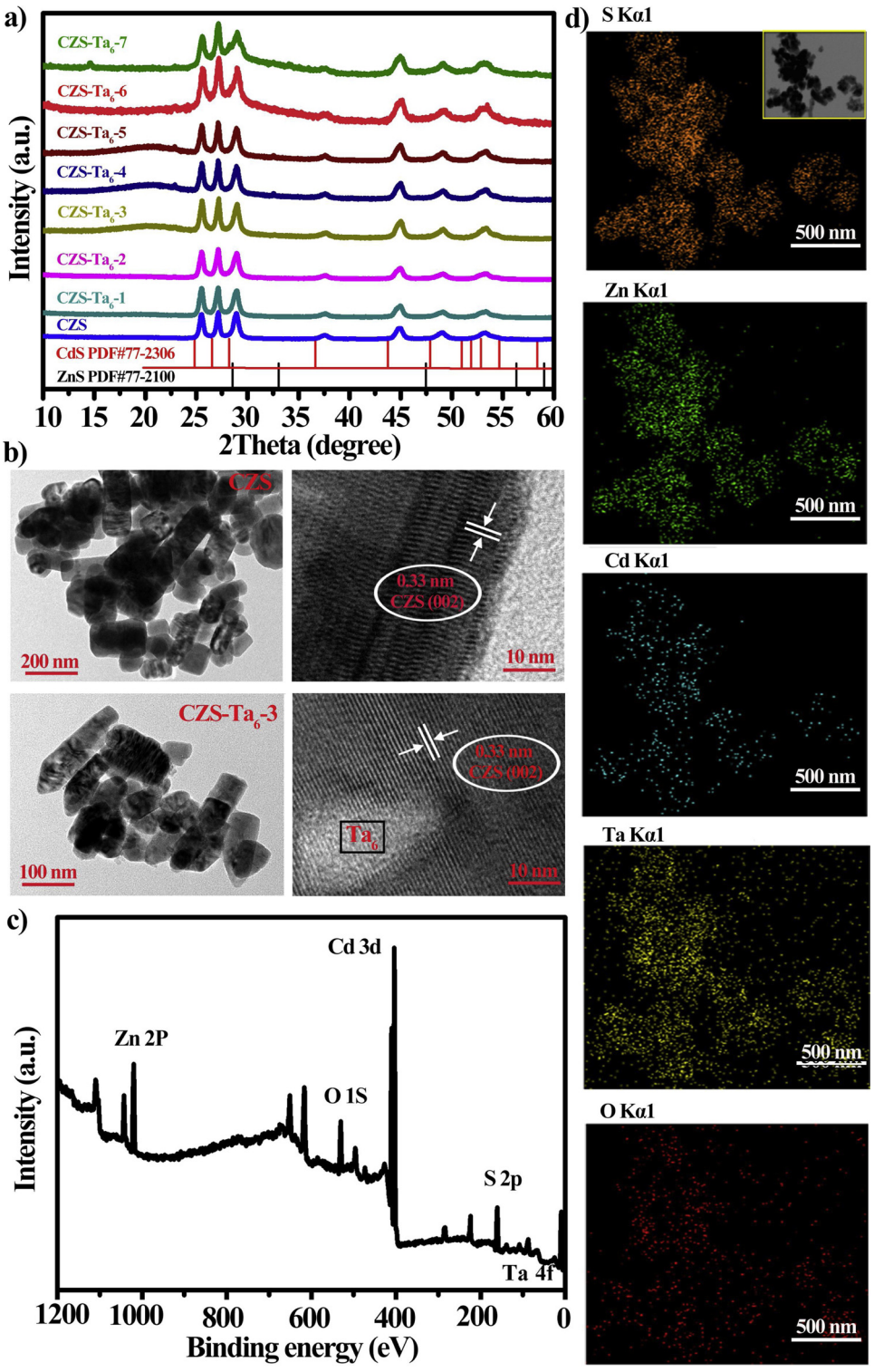

Fig. 1. a) PXRD patterns of CZS and Ta_6 /CZS composites b) TEM, HRTEM images of CZS and Ta_6-3/CZS composite. c) XPS survey spectrum of Ta_6-3/CZS composite. d) Elemental mapping images of Ta_6-3/CZS composite.

of $0.1 - 10^5$ Hz.

3. Results and discussion

3.1. Characterization of Ta_6/CZS

A series of new binary photocatalysts Ta_6/CZS with different Ta_6 loaded amounts (0.025, 0.05, 0.1, 0.25, 0.5, 0.75, 1.0 g) were hydrothermally synthesized and denoted as Ta_6-1/CZS to Ta_6-7/CZS, respectively. Powder X-ray diffraction (PXRD) patterns of CZS exhibits multiphase characteristics in comparison with that of the cubic phase ZnS (JCPDS Card No. 77-2100) and the hexagonal phase CdS (JCPDS Card No. 77-2103) (Fig. 1a), indicating the formation of the CZS solid. The PXRD patterns of Ta_6/CZS are similar to that of pristine CZS, indicating that the crystal structure of CZS can be preserved after it is coupled with Ta_6. No characteristic diffraction peaks associated with

Ta_6 is observed, suggesting that Ta_6 might be highly dispersed on the surface of CZS structure or the relatively low content of Ta_6 makes them hard to identify. Similar phenomena can also be found in other composite materials [35].

As a very sensitive technique for the detection of the vibrations of metal-oxo bonds of POMs, FT-IR measurements were performed to confirm the structural integrity of Ta_6 in the as-prepared Ta_6/CZS composites. The FT-IR spectra of Ta_6/CZS composites are similar to that of pristine CZS except for the two new peaks at 842 and 625 cm^{-1} (Figure S1), which are assigned to the characteristic Ta = O terminal vibration and bridging Ta–O–Ta stretching vibration found in known $[Ta_6O_{19}]^{8-}$ [36]. The FT-IR results confirm that the POTa Ta_6 is successfully introduced into CZS and its structure is well maintained.

The morphology and microstructures of the pristine CZS and the representative Ta_6-3/CZS hybrid sample were investigated by TEM and high resolution TEM (HRTEM). In Fig. 1b, CZS shows the morphology of Inhomogeneous nanorods (NR_S) composed of a high-density parallel distributed strips. The HRTEM image exhibits that CZS NR_S are composed of nonuniform zigzag structures in which the distinct lattice fringes with 0.33 nm spacing can be assigned to the (002) plane of CZS, which is well consistent with the XRD results. The TEM and HRTEM images of the as-synthesized sample Ta_6-3/CZS show that some smaller Ta_6 NPs are distributed and intimately attached on the surface of CZS NR_S, indicating the formation of heterojunctions, which can accelerate the electron–hole separation in the photoexcited carrier process and improve the photocatalytic efficiency [37]. Additionally, the elemental mappings of the Ta_6-3/CZS sample prove that the Cd, Zn, S, O and Ta elements distribute uniformly in the hybrid sample at the nanoscale over the nanorods Fig. 1(d) and the proportion of each metal in the Ta_6-3/CZS is determined by inductively coupled plasma-atomic emission spectrometry (ICP-AES) (Table S1)

The chemical states and the surface composition of the elements were investigated by XPS measurements. As shown in Fig. 1c, the survey spectrum of Ta_6-3/CZS discloses the prescence of Cd, Zn, S, O and Ta, which is well consistent with the elemental mapping results. The high resulotion XPS peaks located at 1042.94, 1019.91, 403.46, 410.18, and 160.13 eV correspond to typical values for Zn $2P_{1/2}$, Zn $2P_{3/2}$, Cd $3d_{5/2}$, Cd $3d_{3/2}$, and S $2p_{3/2}$, respectively (Figure S2) [19,38,39]. While, the Ta $4f_{7/2}$ and $4f_{5/2}$ peaks located at 25.55 and 27.25 eV, respectively, showing the presence of Ta (V) [40]. The XPS results confirm that Ta_6 has been successfully loaded on the surface of CZS without changing the valence of Ta. Notably, slight binding energy shifts, compared with CZS, might derive from the electronic interactions between Ta_6 and CZS (Figure S3).

The textural properties of Ta_6/CZS composite samples were measured by Nitrogen physical adsorption experiments. As shown in Figure S4, the absorption isotherms curve for CZS, Ta_6/CZS samples exhibit typical type IV isotherms. Pristine CZS possesses the BET surface area of 14.53 $m^2 g^{-1}$. By the introduction of Ta_6, the BET surface areas of Ta_6/CZS samples are gradually increased with the increasing Ta_6 loading amount. The highest surface area is observed in Ta_6 -7/CZS (59.47 $m^2 g^{-1}$) (Table S2). Genearlly, a high surface area can increase active reaction sites, thus to facilitate the photocatalytic activity. While, excessive Ta_6 NPs might lead to a reunion phenomenon, which will decrease the photocatalytic activity.

To study the optical properties of CZS, Ta_6, and Ta_6/CZS composite samples, ultraviolet–visible diffuse reflectance spectra (DRS) analysis was carried out. As shown in Fig. 2a, the Ta_6 sample has an absorption at 245 nm in the UV region, with an energy gap estimated to be 4.12 eV. The absorption edge of pristine CZS presents at aroud 505 nm and the corresponding band-gap is caclulated to be 2.46 eV, which is in agreement with the value reported before [41]. Compared to pure Ta_6 sample, the binary Ta_6/CZS sample show intense absorption over a broad range of wavelengths in the visible-light region, leading to the ehancement of solar energy utilization efficiency. Nevertheless, no noticeable shift of the absorption edge can be observed with different Ta_6 loading amounts, revealing that Ta_6 is loaded onto the surface of CZS rather than being doped into the CZS lattice.

3.2. Photocatalytic performance and mechanism

Without using noble metal as a co-catalyst or a photosensitizer, the photocatalytic HER activities of the pristine CZS, Ta_6 and Ta_6/CZS nanocomposites were tested with 0.35 M Na_2S/Na_2SO_3 aqueous solution under visible light irradiation ($\lambda > 420$ nm). A detailed comparison of photocatalytic HER is studied and the results are shown in Fig. 3a. The Hydrogen evolution rates of Ta_6 and pristine CZS are 0.29 and 15.13 mmol $h^{-1} g^{-1}$, respectivley. When Ta_6 and CZS are combined together, the gradually increasing H_2 evolution activities can be observed from Ta_6-1/CZS to Ta_6-3/CZS, and the highest activity of 43.05 mmol $h^{-1} g^{-1}$ found for photocatalyst Ta_6-3/CZS, which is approximately 148.44 and 2.85 times than that of parent Ta_6 and CZS, respectively. A high quantum efficiency of 37% is achieved in the case of Ta_6-3/CZS at 420 nm, which is one of the most highly efficient noble-metal-free metal-sulfide-based photocatalysts (Table S3). In addition, the maximum visible-light-driven H_2 evolution rate (43.05 mmol $h^{-1} g^{-1}$) is much higher than those of all POM-based photocatalysts and most metal-sulfide-based photocatalyts (Table S4 and S5). While, with the increase of Ta_6 content from Ta_6-3/CZS to Ta_6-7/CZS, the H_2 evolution rate gradually decreases. The lowest hydrogen evolution rate is 13.35 mmol $h^{-1} g^{-1}$ observed for Ta_6-7/CZS, which is even slightly lower than that of pristine CZS. The reason may be attributed to the aggregation of overloading Ta_6 on the surface of CZS which prevents CZS from harvesting light [42,43].

To evaluate the stability of the birnary composite photocatalyst Ta_6-3/CZS, recycling tests of photocatalytic H_2 evolution were performed. The results show that Ta_6-3/CZS has high photocatalytic stability with no obvious decrease of H_2 evolution rate at least four recycles in 24 h (Fig. 3b). In addition, the PXRD patterns of Ta_6-3/CZS are no obvious change before and after 4-cycle catalytic reactions (Fig. 3c). The influence of the concentrations of the sacrificial reagent Na_2S/Na_2SO_3 on the photocatalytic HER activity of Ta_6-3/CZS was also investigated. With the concentration of Na_2S/Na_2SO_3 increased from 0.1 M to 0.35 M, the photocatalytic activity of Ta_6-3/CZS is rapidly increased (Fig. 3d). While, a remarkable decrease in the H_2 evolution rate from 43.05 to 17.78 mmol $h^{-1} g^{-1}$ is observed with further increase of the Na_2S/Na_2SO_3 concentration from 0.35 M to 1.0 M, which may be attributed to the loss of light energy blocked by the undissolved Na_2SO_3 particles [44].

It is known that the higher the photocurrent response, the higher the separation efficiency of the photogenerated electron-hole pairs [45]. Therefore, Electrochemical impedance spectroscopy (EIS) and the transient photocurrent response of the as-prepared CZS, Ta_6 and Ta_6/CZS samples were performed to verify the high-performance photocatalytic activity of Ta_6-3/CZS. As shown in Fig. 4a, CZS displays a low photocurrent density (0.31 μA cm^{-2}) under visible-light irradiation and Ta_6 almost doesn't respond to visible light irradiation. In contrast, Ta_6-1/CZS, Ta_6 -5/CZS and Ta_6-3/CZS generate relatively high photocurrent intensities of 0.63, 0.63 and 1.07 μA cm^{-2}, respectively. In particular, the photocurrent intensity of Ta_6-3/CZS is remarkably larger (3.5 times) higher than that of CZS, indicating that the heterojunction effect between CZS and Ta_6 can significantly accelerate the photogenerated charge separation [46,47]. Next, Fig. 4b exhibits the EIS Nyquist plots. The radius of the arc on the EIS Nyquist plot can evaluate the internal resistances for the charge transfer process in the photocatalytic reaction [48,49]. Usually a smaller radius of curvature means a higher carrier mobility rate. It can be found that the radius on Nyquist plots of Ta_6-3/CZS is much smaller than those of CZS and Ta_6, also indicating that Ta_6-3/CZS is the best sample for separating charge carriers and transfering interfacial charge.

Photoluminescence (PL) spectroscopy was put in place to investigate the recombination behaviour of photoinduced electron-hole

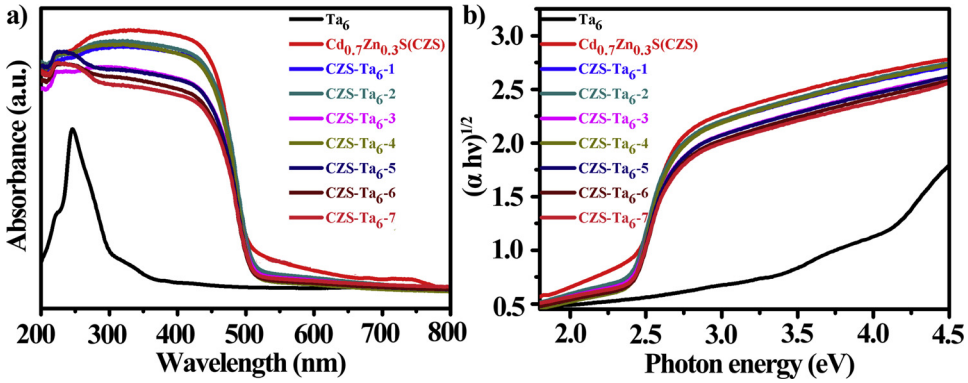

Fig. 2. Ultraviolet–visible diffuse reflectance spectra (a) and band-gap calculation (b) of CZS, Ta_6 and Ta_6/CZS composites.

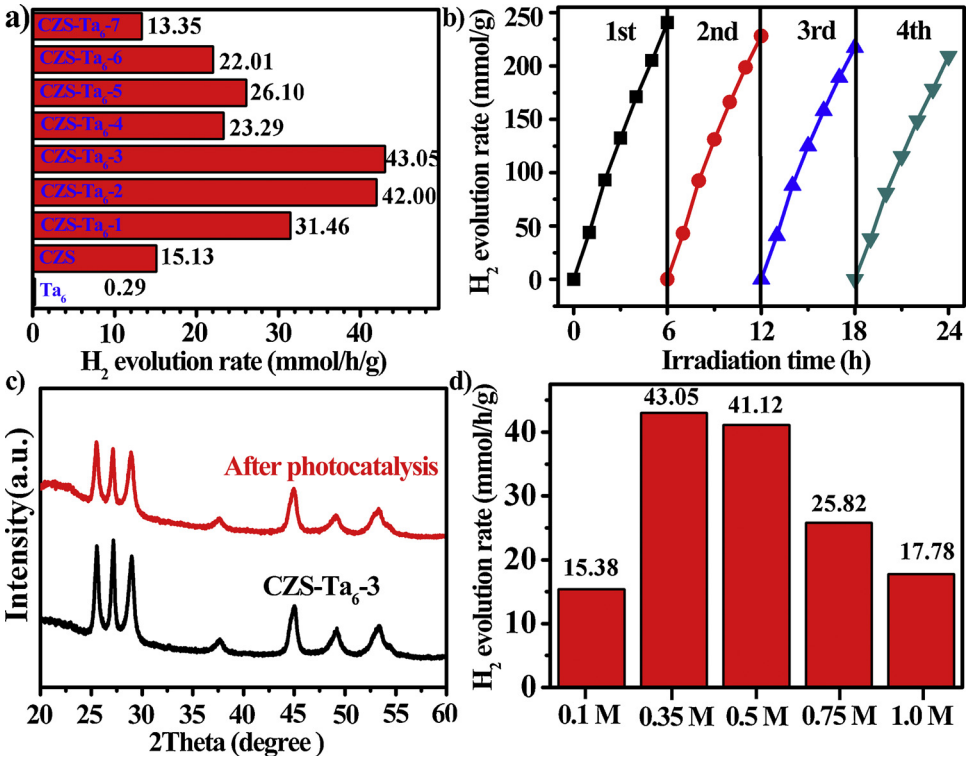

Fig. 3. a) A comparison of the visible-light-driven H_2 evolution rates based on CZS, Ta_6 and Ta_6/CZS as photocatalysts ($\lambda > 420$ nm); b) Four consecutive runs for the H_2 production by using Ta_6-3/CZS as photocatalyst. c) PXRD patterns of Ta_6-3/CZS before and after the photocatalytic H_2 evolution. d) The H_2 evolution rates based on Ta_6-3/CZS as photocatalyst with different Na_2S/Na_2SO_3 concentrations.

pairs. The recombination of free charge carriers can release energy in the form of PL emission. Hence, the remarkable PL quenching may suggest a largly suppressed recombination rate of charge carriers, thereby boosting the photocatalytic activity [5]. As shown in Fig. 4c, the PL intensities of Ta_6/CZS hybrid material decrease remarkably in comparison with that of the parent CZS, evincing that the introduction of Ta_6 can suppress the recombination of photogenerated charge carrier to give better photocatalytic ability.

Based on the above analyses, the possible photocatalytic HER mechanism over Ta_6-3/CZS composite can be deduced as following. The CB and VB edges of Ta_6, denoted as E_{CB} and E_{VB}, are estimated by the equations $E_{VB} = X - E_0 + 0.5\,Eg$ and $E_{CB} = E_{VB} - Eg$ [50], where X, E_0, and Eg are the electronegativity of the semiconductor (ca. 6.39 eV for Ta_6), the energy of the free electrons on the hydrogen scale (approximately 4.5 eV), and the band gap energy of the semiconductor (ca. 4.12 eV For Ta_6), respectively. Following the equations, the E_{CB} and E_{VB} for Ta_6 are -0.17 eV and 3.95 eV vs. SHE. Similarly, the E_{CB} and E_{VB} of CZS are calculated as -0.52 eV and 1.94 eV. As shown in Fig. 5, when the Ta_6/CZS composites are exposed to visible light, the photogenerated electrons of CZS transfer from VB to CB, while the Ta_6 cannot absorb visible light due to its large band gap (4.12 eV). Since the E_{CB} of CZS (-0.52 eV) is more negative than that of Ta_6 (-0.17 eV), the photogenerated electrons on the CB of CZS can be fleetly transfered into the CB of Ta_6, resulting in the effective separation of photoinduced electron-hole pairs. Meanwhile, photoinduced holes migrate from Ta_6 to CZS surface, because the VB of Ta_6 is positioned lower than that of CZS. Besides, the VB of Ta_6 (-0.17 eV) is negative to the redox potential of H^+/H^2 [51], and therefore it can supply abundant surface active sites for photoexcited electrons transfer to generate H_2.

4. Conclusions

In summary, POTa is employed to combine with metal sulfide to synthesize a series of new-type Ta_6/CZS composite photocatalysts by a facile hydrothermal method. These binary heterojunction materials exhibit much more high-performance photocatalytic HER activity than those of all known POM-based photocatalysts and most of known metal sulfide-based photocatalysts. The reasonable mechanism of the Ta_6/CZS composite photocatalysts working under the visible-light irradiation has been proposed. The results firstly reveal that the combination of

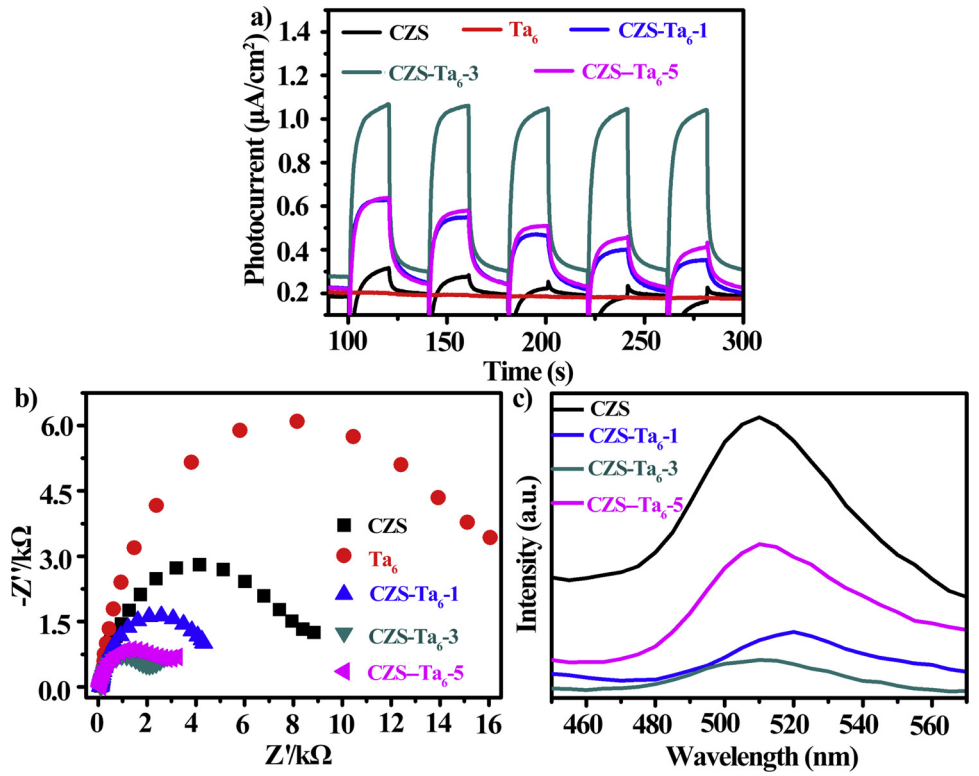

Fig. 4. a) Transient photocurrent responses and b) EIS Nyquist plots of CZS, Ta_6 and Ta_6/CZS. c) Photoluminescence spectra with the excitation wavelength of 340 nm.

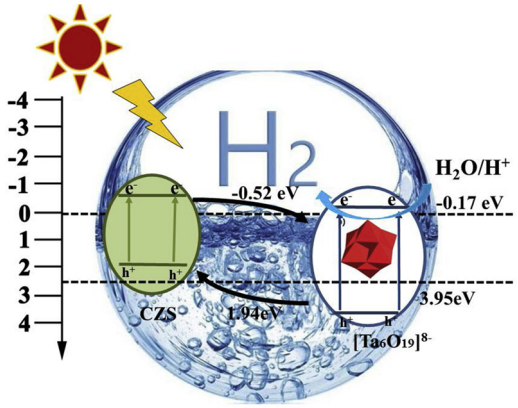

Fig. 5. Proposed possible mechanism schematic of Ta_6/CZS composite.

POTas and metal sulfides can form promising, highly effective photocatalysts for photocatalytic HER from water. Considering that there are various POTas with different structures, sizes, charges and compositions as well as unique redox properties, this work might open a promising avenue in producing diverse, new-type, and more efficient POTa/metal sulfide heterojunction photocatalysts for solar energy utilization by water splitting, CO_2 fixation and organosynthesis.

Acknowledgements

The financial support of the National Natural Science Foundation of China (grant no. 21773029) and 111 Project.

Appendix A. Supplementary data

Supplementary material related to this article can be found, in the online version, at doi:https://doi.org/10.1016/j.apcatb.2019.02.052.

References

[1] H.B. Gray, Nat. Chem. 1 (2009) 7.
[2] J.S. Hu, L.L. Ren, Y.G. Guo, H.P. Liang, A.M. Cao, L.J. Wan, C.L. Bai, Angew. Chem. Int. Ed. 44 (2005) 1269–1273.
[3] L.Z. Wu, B. Chen, Z.J. Li, C.H. Tung, Acc. Chem. Res. 47 (2014) 2177–2185.
[4] M.D. Regulacio, M.Y. Han, Acc. Chem. Res. 49 (2016) 511–514.
[5] A. Kudo, Y. Miseki, Chem. Soc. Rev. 38 (2009) 253–278.
[6] T. Hisatomi, J. Kubota, K. Domen, Chem. Soc. Rev. 43 (2014) 7520–7535.
[7] W.J. Ong, L.L. Tan, Y.H. Ng, S.T. Yong, S.P. Chai, Chem. Rev. 116 (2016) 7159–7329.
[8] X.C. Wang, K. Maeda, A. Thomas, K. Takanabe, G. Xin, J.M. Carlsson, K. Domen, M. Antonietti, Nat. Mater. 8 (2009) 76–80.
[9] G.G. Zhang, L.H. Lin, G.S. Li, Y.F. Zhang, A. Savateev, S. Zafeiratos, X.C. Wang, M. Antonietti, Angew. Chem. Int. Ed. 57 (2018) 9372–9376.
[10] H.H. Ou, P.J. Yang, L.H. Lin, M. Anpo, X.C. Wang, Angew. Chem. Int. Ed. 56 (2017) 10905–10910.
[11] G.G. Zhang, G.S. Li, Z.A. Lan, L.H. Lin, A. Savateev, T. Heil, S. Zafeiratos, X.C. Wang, M. Antonietti, Angew. Chem. Int. Ed. 56 (2017) 13445–13449.
[12] G.G. Liu, T. Wang, H.B. Zhang, X.G. Meng, D. Hao, K. Chang, P. Li, T. Kako, J.H. Ye, Angew. Chem. Int. Ed. 54 (2015) 13561–13565.
[13] M.C. Liu, L.Z. Wang, G.Q. Lu, X.D. Yao, L.J. Guo, Energy Environ. Sci. 4 (2011) 1372–1378.
[14] Y.G. Chen, S. Zhao, X. W ang, Q. Peng, R. Lin, Y. Wang, R.G. Shen, X. Cao, L.B. Zhang, G. Zhou, J. Li, A.D. Xia, Y.D. Li, J. Am. Chem. Soc. 138 (2016) 4286–4289.
[15] M.C. Liu, D.W. Jing, Z.H. Zhou, L.J. Guo, Nat. Commun. 4 (2013) 2278.
[16] Y.F. Yu, J. Zhang, X. Wu, W.W. Zhao, B. Zhang, Angew. Chem. Int. Ed. 51 (2012) 897–900.
[17] Y.G. Chen, S. Zhao, X. Wang, Q. Peng, R. Lin, Y. Wang, R.G. Shen, X. Cao, L.B. Zhang, G. Zhou, J. Li, A.D. Xia, Y.D. Li, J. Am. Chem. Soc. 138 (2016) 4286–4289.
[18] M.C. Liu, Y.B. Chen, J.Z. Su, J.W. Shi, X.X. Wang, L.J. Guo, Nat. Energy 1 (2016) 16151.
[19] X.X. Zhao, J.R. Feng, J. Liu, W. Shi, G.M. Yang, G.C. Wang, P. Cheng, Angew. Chem. Int. Ed. 57 (2018) 9790–9794.
[20] J. Zhang, L.F. Qi, J.R. Ran, J.G. Yu, S.Z. Qiao, Adv. Energy Mater. 4 (2014) 1301925.
[21] X. Wu, Y.F. Yu, Y. Liu, Y. Xu, C.B. Liu, B. Zhang, Angew. Chem. Int. Ed. 51 (2012) 3211–3215.
[22] S.R. Lingampalli, U.K. Gautam, C.N.R. Rao, Energy Environ. Sci. 6 (2013) 3589–3594.
[23] L. Jin, X.X. Li, Y.J. Qi, P.P. Niu, S.T. Zheng, Angew. Chem. Int. Ed. 55 (2016) 13793–13797.

[24] Z. Li, X.X. Li, T. Yang, Z.W. Cai, S.T. Zheng, Angew. Chem. Int. Ed 56 (2017) 2664–2669.
[25] T. Tachikawa, S. Tojo, M. Fujitsuka, T. Majima, Chem. Eur. J. 12 (2006) 3124–3131.
[26] M.T. Pope, A. Muller, Angew. Chem. Int. Ed. 30 (1991) 34–48.
[27] H. Lia, S. Yao, H.L. Wu, J.Y. Qu, Z.M. Zhang, T.B. Lu, W.B. Lin, E.B. Wang, Appl. Catal. B Environ. 224 (2018) 46–52.
[28] P. Huang, X.J. Wang, J.J. Qi, X.L. Wang, M. Huang, H.Y. Wu, C. Qin, Z.M. Su, J. Mater. Chem. A.5 (2017) 22970–22974.
[29] X.J. Kong, Z.K. Lin, Z.M. Zhang, T. Zhang, W.B. Lin, Angew. Chem. Int. Ed. 55 (2016) 6411–6416.
[30] B. Matt, J. Fize, J. Moussa, H. Amouri, A. Pereira, V. Artero, G. Izzet, A. Proust, Energy Environ. Sci. 6 (2013) 1504–1508.
[31] S.J. Li, S.M. Liu, S.X. Liu, Y.W. Liu, Q. Tang, Z. Shi, S.X. Ouyang, J.H. Ye, J. Am. Chem. Soc. 134 (2012) 19716–19721.
[32] P. Huang, C. Qin, Z.M. Su, Y. Xing, X.L. Wang, K.Z. Shao, Y.Q. Lan, E.B. Wang, J. Am. Chem. Soc. 134 (2012) 14004–14030.
[33] Z.Y. Zhang, Q.P. Lin, D. Kurunthu, T. Wu, F. Zuo, S.T. Zheng, C.J. Bardeen, X.H. Bu, P.Y. Feng, J. Am. Chem. Soc. 133 (2011) 6934–6937.
[34] M. Filowitz, R. Ho, W.G. Klemperer, W. Shum, Inorg. Chem. 18 (1979) 93–103.
[35] M.Y. Liu, H. Chen, H.M. Zhao, Y.F. He, Y.H. Li, R. Wang, L.C. Zhang, W.S. You, Dalton Trans. 46 (2017) 9407–9414.
[36] J.H. Son, W.H. Casey, Chem. Eur. J. 22 (2016) 14155–14157.
[37] J. Zhang, J. Yu, Y. Zhang, Q. Li, J.R. Gong, Nano Lett. 11 (2011) 4774–4779.
[38] M. Imran, A.B. Yousaf, P. Kasak, A. Zeb, S.J. Zaidi, J. Catal. 353 (2017) 81–88.
[39] W. Zhang, Y.B. Wang, Z. Wang, Z.Y. Zhong, R. Xu, Chem. Commun. 46 (2010) 7631–7633.
[40] X. Yu, Z.H. Li, J.W. Liu, P.H. Hu, Appl. Catal. B Environ. 205 (2017) 271–280.
[41] Q. Li, H. Meng, P. Zhou, Y.Q. Zheng, J. Wang, J.G. Yu, J.R. Gong, ACS Catal. 3 (2013) 882–889.
[42] C. Li, Y. Du, D. Wang, S. Yin, W. Tu, Z. Chen, M. Kraft, G. Chen, R. Xu, Adv. Funct. Mater. 27 (2017) 1604328.
[43] D.P. Kumar, E.H. Kim, H. Park, S.Y. Chun, M. Gopannagari, P. Bhavani, D.A. Reddy, J.K. Song, T.K. Kim, ACS Appl. Mater. Interfaces 10 (2018) 26153–26161.
[44] Z.J. Sun, H.F. Zheng, J.S. Li, P.W. Du, Energy Environ. Sci. 8 (2015) 2668–2676.
[45] C.L. Yu, W.Q. Zhou, L.H. Zhu, G. Li, K. Yang, R.C. Jin, Appl. Catal. B Environ. 184 (2016) 1–11.
[46] Y. Wang, Y.Z. Zheng, S.Q. Lu, X. Tao, Y.K. Che, J.F. Chen, ACS Appl. Mater. Interfaces 7 (2015) 6093–6101.
[47] H.L. Wang, L.S. Zhang, Z.G. Chen, J.Q. Hu, S.J. Li, Z.W. Wang, J.S. Liu, X.C. Wang, Chem. Soc. Rev. 43 (2014) 5234–5244.
[48] S.J. Yu, H.J. Yun, Y.H. Kim, J. Yi, Appl. Catal. B Environ. 144 (2014) 893–899.
[49] C. Lei, F. Han, D. Li, W.C. Li, Q. Sun, X.Q. Zhang, A.H. Lu, Nanoscale 5 (2013) 1168–1175.
[50] M.A. Butler, D.S. Ginley, J. Electrochem. Soc. 125 (1978) 228–232.
[51] P.F. Wang, S.H. Zhan, H.T. Wang, Y.G. Xia, Q.L. Hou, Q.X. Zhou, Y. Li, R.R. Kumar, Appl. Catal. B Environ. 230 (2018) 210–219.